

Analysis of X-ray spectra on DPPC bilayers

D. Finocchiaro¹, U. Wanderlingh¹

¹Department of physics and earth sciences, University of Messina

E-mail: danilofinocchiaro@hotmail.it

Abstract

Cells membranes are very complex systems, characterized by a big number of different biological components embedded in a bilayer structure of phospholipids. To understand function and connexions between components it is useful to start from a very simple membrane model: an “artificial” bilayer formed by only one phospholipid (DPPC). X-ray diffraction at small angle is the ideal tool to characterize the structure of the bilayer. In this paper we present a calculation of the electron density profile along the bilayer normal direction: (z), for an hydrated DPPC bilayer at different temperature. Through this analysis we also extract some parameters associated to self-organization of DPPC.

Keywords: DPPC, X-ray diffraction, membrane models.

Introduction

Membrane is the basic organ in the constitution of cells. It defends and separates cell from external environment, assuring ideal conditions to biochemistry of life. Through the particoular membrane structure the cell is able to have a selective interaction with environment. Mobility of its constituents permits an optimal adapting capability to different external conditions.

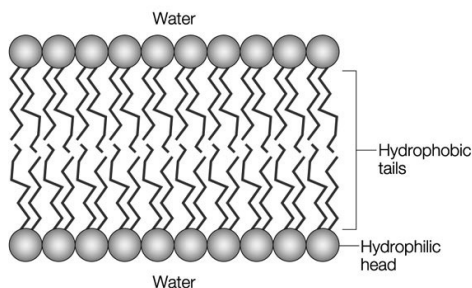


Figure 1: Phospholipid bilayer structure

The central core of any biological membrane is formed by phospholipids, amphiphilic molecules composed composed of two fatty acids, a glycerol unit, a phosphate group and a polar molecule. The phosphate group and polar head region of the molecule is hydrophilic, while the fatty acid tail is hydrophobic. When placed in water, phospholipids will orient themselves side by side to form a lipid bilayer with head groups turned towards the surrounding water and apolar acyl chains in the membrane interior.

Phospholipid bilayers exhibit lyotropic liquid

crystalline properties and present a variety of structural phases as temperature is changed. From low to high temperatures [1], they pass from an highly ordered crystal/subgel phase L_c , to a gel phase (L_β) which shows little disorder; then a fluid phase (L_α) is approached which shows a liquid-like disorder throughout the whole system (two-dimensional fluid). Just below L_α , a ripple phase (P_β) is found in which the lamellar structure is deformed by periodic modulations.

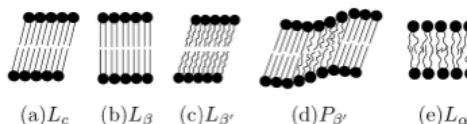


Figure 2: Schematical drawings of the various bilayer phases [7]

Natural membranes are too complex systems to be investigated by physical techniques in order to understand the relationship between the structure and dynamics of the system and the membrane functions. A simpler model membrane can be realized by an artificial assembling of one type of phospholipid arranged in a multi-bilayer structure in an aqueous environment.

A widely used model membrane [1–3] is based on Dipalmitoylphosphatidylcholine (DPPC), a phospholipid consisting of two palmitic acid tails and a phosphatidylcholine head group. In living organism DPPC is the major constituent of pulmonary surfac-

tant.

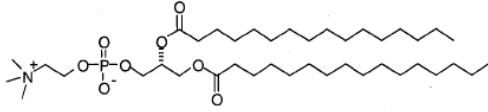


Figure 3: DPPC molecule

Structural information on the bilayer structure can be obtained by X ray diffraction at small angle. By means of this techniques it is possible to determine the spatial ordering of the lamellar structure (inter bilayer ordering) and molecular structure inside the bilayer. This can be achieved via the determination of the electron density profiles along bilayer normal. Moreover a study in function of the temperature can provide important information about the different organization of the phospholipids in the liquid crystalline and gel phases.

Materials and methods

Highly ordered multi-bilayers samples of DPPC (purchased from Avanti Polar Lipids) were obtained following the preparation suggested by Hallock et al [4]. Samples were prepared on a Silicon wafer (thickness: $250\mu\text{m}$) as substrate, depositing about 1.5 mg of lipids per cm^2 .

Accordingly to the cited procedure each mg of lipids it was dissolved in $50\mu\text{l}$, $2 : 1\text{CHCl}_3/\text{CH}_3\text{OH}$ containing a 1:1 molar ratio of naphthalene. The solution was then spread on the substrate plates and dried under Nitrogen flux. To remove the naphthalene and any residual organic solvent, the samples were vacuum dried overnight. After samples were indirectly hydrated at 550°C in 96% relative humidity using a saturated potassium sulfate H_2O solution for 12 days, after which about 18 mole of H_2O per mole of lipid were added. The plates were eventually let to equilibrate at 4°C for an additional 10 days.

The use of Si wafer cut on the (4:0:0) plane as supporting substrate present the advantage of a zero background in the angular range of interest, and shows a well defined peak at $2\theta = 69.131^\circ\text{C}$, that was used as a reference to calibrate the sample vertical position in the scattering geometry.

In order to control temperature and humidity samples were hosted in a small chamber with a Kapton window during the measurements. Each scan covered 2θ from 0.9 to 20°C with step size of 0.02°C , one second per step. Temperature stability was controlled by a PT100 and the humidity was adjusted by adding water into an open reservoir. A stream of heated air was flushed to the top of the chamber to prevent formation of vapour inside the chamber

which may condensate over the sample and disturb the measurements.

X-Ray diffraction measurements were performed with a D8-ADVANCE Bruker diffractometer in the Bragg-Brentano geometry using the $\text{Cu K}\alpha_1$ line ($\lambda = 1.542\text{ \AA}$). The diffraction patterns was collected in the Bragg-Brentano geometry, thus allowing to directly obtain information in the direction normal to the bilayer planes.

Theory and data analysis

When X-rays reflect on a surface, we detect a inhomogeneous pattern due to interference phenomena (Bragg reflection). We observe intensity maxima when is satisfied the Bragg law:

$$n\lambda = 2d\sin\theta \quad (1)$$

n is an integer, λ the X-ray wavelength, θ the detection angle and d the spacing between diffraction planes.

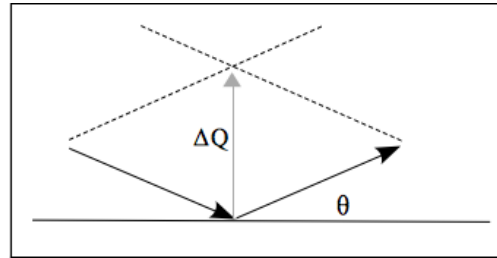


Figure 4: Bragg geometry example

Well known theory suggest us that the output spectrum is the product of two parts: a form factor $F(q)$ and a structure factor $S(q)$. The former is related to Fourier Transform of single bilayer electron density, the second is linked to membranes overlapping geometrical structure (as we said, samples was composed by a number of bilayers overlapping on a silicon layer).

$$F(q) = \int_{-D/2}^{D/2} \rho(z)e^{-iqz} dz \quad (2)$$

Because the momentum ΔQ is normal to bilayer, the electron density described by shape factor has to be considered along this direction (we call it z). X-ray spectrum will then be:

$$I(q) = S(q) \frac{|F(q)|^2}{q} \quad (3)$$

where the factor $1/q$ is the Lorentz factor correction applied for oriented samples.

A simple way to divide these contributes is to consider that $S(q)$ is produced by an ordered succession

of bilayers, then it will be composed by a series of sharp peaks, their spacing will be $\Delta q = 2\pi/d$, where d is physical spacing between bilayers.

In $I(q)$ then we can see only $F(q)$ points corresponding to $S(q)$ peak centers. $F(q)$ value will be the area under corresponding peak.

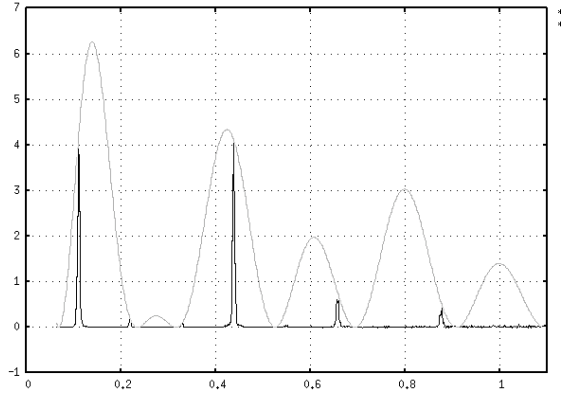


Figure 5: Comparison between $I(q)$ (black line) and $F(q)^2$ (gray line); abscissa and ordinate unit are respectively \AA^{-1} and counts

Comparing other experiences [1] [2] [3], we choose a mathematical model for the electron density of bilayer: the 2G model, that is composed by four terms: 3 gaussians (representing phospholipid head, organic chains and methyl tails) and a baseline used to match mean electron density values at the center and out of the bilayer (see fig 6).

To reconstruct electron density we have written a Fortran implementation that calculates the electron density 2G model TF and compare it to experimental data.

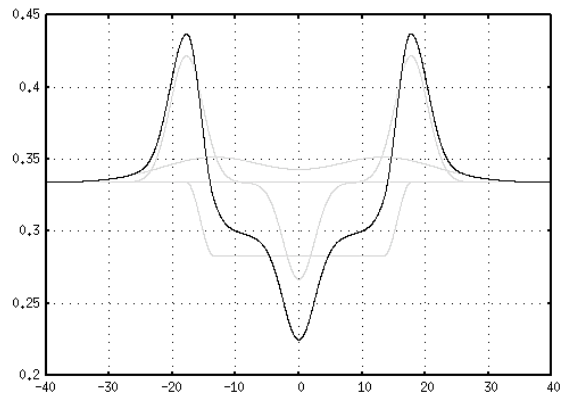


Figure 6: $\rho(z)$ 2G model; the gray lines are the four contributions (three gaussians and the baseline), the black one is total electron density

Before start the analysis it is necessary to elaborate the experimental spectrum: this was done in

three steps:

-Using the silicon peak reference to translate the low-angle spectrum. An incorrect sample vertical placement in fact produce a q shift of the spectrum

-Applying Lorentz correction factor $1/q$ for oriented samples

-Calculating all areas under peak to determine $F(q)$.

The experimental spectra have few peaks (4-6), then few shape factor points are available to analysis. Because number of fit parameters is 9 (8 parameter for gaussians + 1 scale factor R), the fit is very sensitive about start conditions. To improve the consistence of final results, we have then start fitting trough parameter values known from literature[1] [2] [3].

Results and discussion

From fit data we have calculated area for lipid A_L varying T . As we know in fact:

$$N_e = A_L \int_0^{D/2} \rho_{el}(z) dz \quad (4)$$

where $N_e = 406$ is number electron per lipid, D the width of bilayer and $\rho_{el}(z)$ is the electron density. D was determined evaluating the least distance in which the three gaussians decay to zero. Considering $\rho_{el}(z)$ typical conformation that we have obtained (see 6) we assume that $D/2 = z_2 + 2\sigma_2$. A_L and D values are displayed in Table .

$T(^{\circ}C)$	$A_L(\text{\AA}^2)$	$D(\text{\AA})$
15	54.47	22.82
20	51.96	24.11
25	52.43	24.71
30	36.09	32.68
35	37.36	30.70
40	37.91	31.70
45	37.73	32.21
55	34.85	34.17

Figure 7: Area per lipid and bilayer thickness varying T

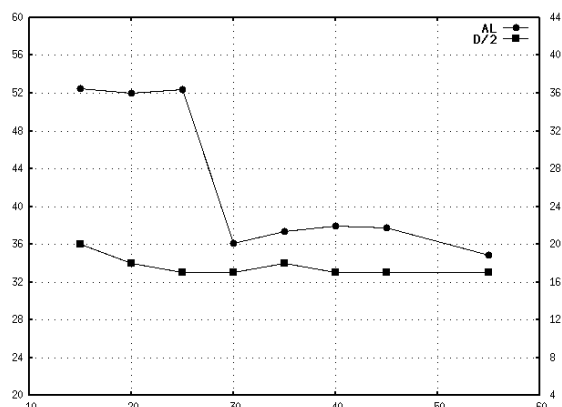


Figure 8: Area per lipid (rounds) and bilayer half-width (squares) varying T ; abscissa and ordinate units are respectively $^{\circ}\text{C}$ and \AA^2 (left), \AA (right)

We can observe a clear change in structural conformation between 25 and 30°C : the bilayer increases its width and area per lipid decreases. These trends could be linked to a change in lipids spaces reorganization. It is possible to calculate volume per lipid and verify that in this thermic range it is near to be constant, suggesting that the thermic restructuring we are observing consists simply of internal lipid structural rearrangements, not involving directly interaction between different lipids. Moreover literature data GEL locate DPPC fluid-gel transition near to 40°C , confirming that we aren't observing this phenomenon. A_L and $D/2$ observed changes could be more probably associated with transition to ripple phase P_{β} called lipid pre-transition. It is located near 35°C and characterized by a rippling of the membrane surface. Further analysis will must be carry on to verify hypothesis truth.

Conclusions

We have been approaching to X-ray analysis of biological membrane model system, starting with DPPC membranes, well known in literature GEL. Fitting

X-ray spectra we have been able to calculate bilayer thickness and area per lipid on the membrane surface, regognizing a possible structural change between 30°C and 35°C . It isn't associabile to the fluid-gel DPPC transition, that occurs near 40°C , but probably it is the so called lipid pre-transition. Further analysis will be however carry on.

References

- [1] Tristram-Nagle, S., Nagle, J.F.: *Lipid bilayers: thermodynamics, structure, fluctuations, and interactions*. Chem. and Phys. of Lipids, **127**, 2004, p. 3–14.
- [2] Wiener, M. C., Suter, R. M., Nagle, J. F.: *Structure of the fully hydrated gel phase of dipalmitoylphosphatidylcoline*. Biophys. J., **55**, 1989, p. 315–325.
- [3] Tristram-Nagle, S., Yufeng, L., Legleiter, J., Nagle, J.F.: *Structure of gel phase DMPC determined by X-ray diffraction*. Biophys. J., **83**, 2002, p. 3324–3335.
- [4] Hallock, J. K., Wildman, Lee, D. K., Ramamoorthy, A.: *An Innovative Procedure Using a Sublimable Solid to Align Lipid Bilayers for Solid-State NMR Studies*. Biophys. J., **82**, 2002, p. 2499–2503.
- [5] Wanderlingh, U., D'Angelo, G., Conti Nibali, V., Crupi, C., Rifici, S., Corsaro, C., Sabatino, G.: *Interaction of alcohol with phospholipid membrane: NMR and XRD investigations on DP-PChexanol system*. Spectroscopy, **24**, 2010, p. 375.
- [6] Rifici, S., Crupi, C., D'Angelo, G., Di Marco, G., Sabatino, G., Conti Nibali, V., Trimarchi, A., Wanderlingh, U.: *Effects of a short length alcohol on the dimyristoylphosphatidylcholine system*. Philosophical Magazine, **91**, 2011, p. 2014–2020.
- [7] Kranenburg, M., Smit, B.: *Phase Behaviour of model lipid bilayers*. J. Phys. Chem. B, **109**, 2005, p. 6553–6563.

Experimental Investigations on Carboxylate-modified Polystyrene Aqueous Solutions by Photon Correlation Spectroscopy

A. Magazzú¹, S. Magazú¹

¹Department of physics and earth science, University of Messina, Messina, Italy

E-mail: magazzua@unime.it

Abstract

Photon Correlation Spectroscopy (PCS) dates back to early 1900, when it was felt that the temporal fluctuations of the intensity of the light scattered by a colloidal suspension were due to Brownian motion of the particles. PCS has become a powerful technique for studying the properties of suspension and solution of colloids, macromolecules and polymers. This technique is widely used to determine the distribution profile of the sizes of small particles in suspension. In this contribution, experimental results of PCS measurements on two different kinds of latex beads are reported. Latex beads are monodispersed polymeric particles and have been diluted in an aqueous medium. They represent a standard calibration system used in several fields due to their size accurately known.

Keywords: photon correlation spectroscopy, dynamic light scattering.

Introduction

During a light scattering event a beam of photon impinges the material and it is scattered by its particles.

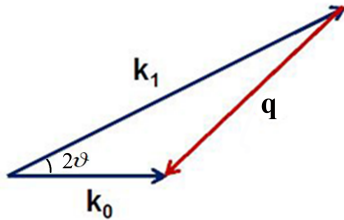


Figure 1: Inelastic scattering, $\mathbf{k}_i \neq \mathbf{k}_f$ and the scattering wavevector \mathbf{q} will also depend on the energy of the scattered photons .

The amplitude of scattered electric field will depend on several quantities including the scattering wavevector $\mathbf{q} = \mathbf{k}_i - \mathbf{k}_f$. During the scattering process photons can transfer part of their energy to the system, this kind of scattering is noted as inelastic and the scattered light will depend on the amount of the energy transferred to the system. During an event of inelastic scattering the modules of wavevector \mathbf{k}_i and \mathbf{k}_f , associated respectively with the incident and scattered photons, are different (Fig. 1) and the scattering wavevector \mathbf{q} will also depend on the energy of the scattered photons.

During a PCS experiment the energy of the scattered photons is almost equal to that of the incident photons ($E_i - E_f \simeq 10^{-3}$) so one can assume that no energy is transferred to the system. This kind

of scattering is known as elastic, \mathbf{k}_i is equal to \mathbf{k}_f and \mathbf{q} will depend only on the incident wavelength λ and on the scattering angle 2ϑ as reported in Fig. 2.

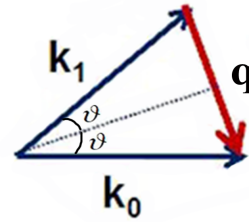


Figure 2: Elastic scattering, $\mathbf{k}_i = \mathbf{k}_f$ and the scattering wavevector \mathbf{q} will depend only on the incident wavelength and on the scattering angle 2ϑ .

$$q = 2k_0 \sin \vartheta = \frac{4\pi \sin \vartheta}{\lambda} \quad (1)$$

Photon Correlation Spectroscopy (PCS) is a light scattering technique commonly employed, not only in Physics, for the investigation of particles undergoing diffusional motion. This technique is widely used to determine the sizes distribution profile of small particles in suspension. When a laser beam impinges a solution containing small particles compared to the laser wavelength, it is possible to observe that the intensity of the scattered light presents some temporal fluctuations caused by constructive and destructive interferences of the light scattered by the particles. These interferences are due to the motion of the particles, often assumed to be random as a result of Brownian motion. Within these intensity fluctuations the

information about the time scale of the movements of the scatterers are contained and these fluctuations can be characterized by an autocorrelation function of the intensity which quantifies how the intensity fluctuations remain correlated over time.

Experimental setup

All PCS data have been obtained in the homodyne mode with a photon-counting detection procedure and a brookhaven BI20-30 AT Digital correlator for the analysis of the scattered light. The light source was a vertically polarized Ar⁺ laser with wavelength of 4880 Å, Ion Pure Plasma Tube INNOVA 70 model, working in the power range of 50-400mW.

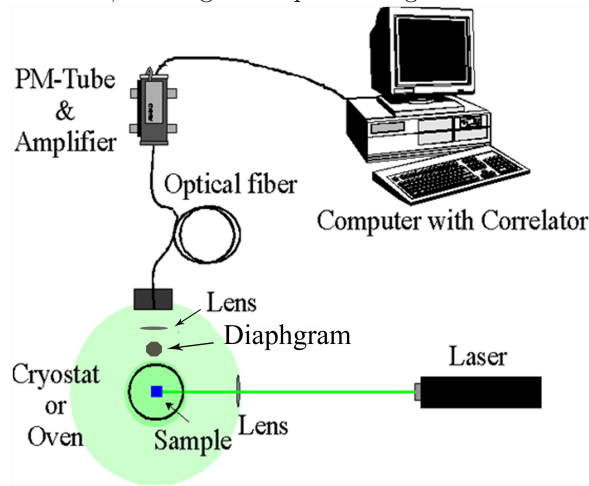


Figure 3: Scheme of the experimental setup of a PCS instrument.

The optical apparatus is mounted on a home-made two arms device, and the angle between the two arms, during these measurements was 90°. The laser beam outcoming the INNOVA 70 was focused by a lens on the sample sited in a sample holder that is interfaced with an heater and a cryostat. The light scattered by the sample passes through a diaphragm that selects the intensity of the scattering light and allows a rough selection of the selected angle with the purpose of avoiding the spurious light collection. The scattered light after passing through the diaphragm is focused on an optical fibre located beyond a pin hole. The optical fibre carries the scattered photons to the phototube. Data signals are then processed by a digital correlator that produces the autocorrelation function of the scattered intensity. The previous experimental setup is depicted in the following scheme (Fig. 3).

Standards used for the calibration of the instrument were two latex beads water solutions of different molecular weight, made of carboxylate-modified polystyrene in aqueous suspension, furnished by

Sigma-Aldrich and with a nominal diameter of 90 and 900 nm respectively. The calibration solutions were prepared with ultrapure and bi-distilled H₂O. All the measurements were performed at room temperature (T=25°C) in a dark environment in order to minimize the spurious light collection. Great care was taken in order to obtain solutions clear and dust-free.

3. Discussion

It is well known [1] that under the assumption that the number of scattering events is large enough that the propagation of the photons is completely random, but small enough to prevent multiple scattering by a single photon, the quantity measured in PCS experiments is the second-order normalized autocorrelation function, defined as:

$$g_2(\mathbf{q}, t) = \frac{\langle I(\mathbf{q}, 0)I(\mathbf{q}, t) \rangle}{\langle I(\mathbf{q}) \rangle^2} \quad (2)$$

The second-order normalized autocorrelation function is related to the autocorrelation function of the scattered electric field by the Siegert's relation:

$$g_2(\mathbf{q}, t) = 1 + \alpha |g_1(\mathbf{q}, t)|^2 \quad (3)$$

where α is an instrumental constant that is between 0 and 1 and g_1 is the normalized autocorrelation function of the electric field, defined as:

$$g_1(\mathbf{q}, t) = \frac{\langle E_S^*(\mathbf{q}, 0)E_S(\mathbf{q}, t) \rangle}{\langle I(\mathbf{q}) \rangle} \quad (4)$$

Where E_S is the scattered electric field. In the case of monodisperse spherical scatters we have that:

$$g_1(\mathbf{q}, t) = \exp(-\Gamma t) = \exp(-D_T \mathbf{q}^2 t) \quad (5)$$

with

$$\Gamma = \frac{1}{\tau} = D_T \mathbf{q}^2 \quad (6)$$

where D_T is the translational diffusion coefficient and $\tau = 1/\Gamma$ is the decay constant. Recalling the Einstein -Stokes relation:

$$D_T = \frac{k_B T}{6\pi\eta R_H} \quad (7)$$

where k_B is the Boltzmann constant, η is the viscosity of the medium, R_H is the hydrodynamic radius, T is the temperature. It is possible to note how in a PCS experiment, one can obtain information about the hydrodynamic diameter of the sample. The translational diffusion coefficient depends not only on the size of the particle core, but also on

any surface structure, as well as the concentration and type of ions in the medium. This means that the size can be larger than that measured by electron microscopy, where the particle is removed from its native environment. In Fig. 4, 5 the $G^{(2)}(t_d)$ for the solutions of latex 900 nm and 90 nm respectively are reported. Black points indicate experimental data, while the red lines represent the result obtained by employing a single exponential fit. For both samples was used the following single exponential function :

$$y(t_d) = A1 \exp(-2(t_d)/t1) + y0 \quad (8)$$

where t_d is the time delay, $A1$ is an instrumental constant, $y0$ is the baseline that is equal to $\langle I \rangle^2$ and $t1$ is the characteristic time decay.

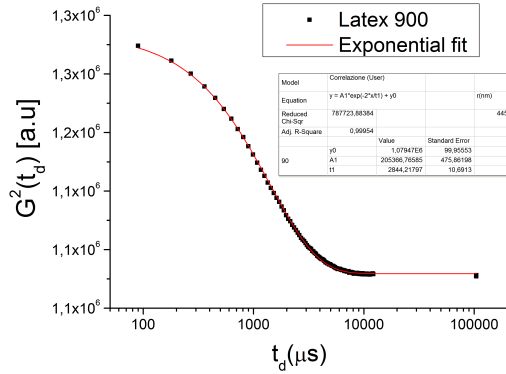


Figure 4: Exponential decay of the $G^{(2)}(t_d)$ for a sample of 900 nm latex beads in aqueous solution, black points indicates experimental data and red line represent a single exponential fit.

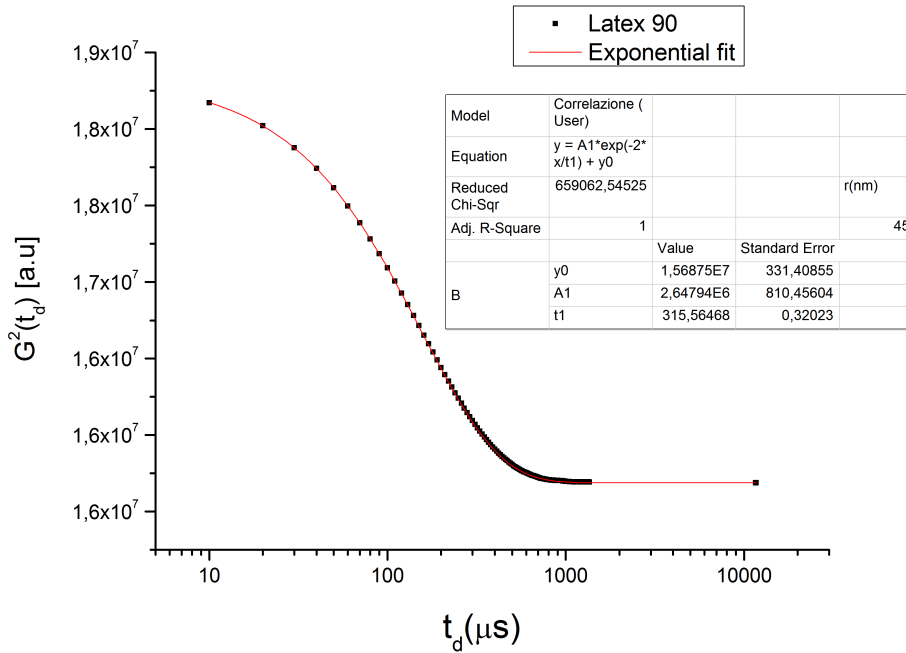


Figure 5: Exponential decay of the $G^{(2)}(t_d)$ for a sample of 90 nm latex beads in aqueous solution, black points indicates experimental data and red line represent a single exponential fit.

Both experimental data of $G^{(2)}(t_d)$ follow an exponential decay as expected from the theory and lead to a diameter that agree with the diameter of the producer of the latex beads.

References

- [1] Dynamic light Scattering with applications to Chemistry, Biology and Physic; Buce.J.Berne and Robert Pecora

Measurement of wet-ability in biocompatible material surfaces

C. Scolaro¹, L. Torrisi¹, M. Cutroneo¹, F. Caridi¹

¹Università di Messina, Dipartimento di Fisica e Scienze della Terra, F. S. D'Alcontres, 98166 S. Agata-Messina, Italy

E-mail: cscolaro@unime.it

Abstract

Measurements of wet-ability of liquid drops using biocompatible solutions, have been performed on different polymers (PMMA, PTFE, PE,...), ceramics (SiO₂, Alumina, Glassy carbon,...) and metals (TiO₂, AISI 304 L, Ti₆Al₄V,...). Surface treatments by using laser beams have been employed to modify the wet-ability. Results put in evidence the best materials to increase or to reduce the wet-ability of the biological liquid. This permits to build biocompatible surfaces to be inserted permanently or to be inserted temporarily in human body. Laser irradiations, depending on the laser intensity and wavelength, permit to change drastically the wet-ability of many materials and to enhance their biocompatibility and functionality. Results will be presented and discussed in detail with special regard to their applications in biological environment where the materials can be embedded.

Keywords: wet-ability, biocompatible material, laser, roughness .

Introduction

The number of applications of biomaterials which have responded to the need to replace or supplement human tissues and organs, not the most active in terms of functional or metabolic damaged by disease or traumatic events has grown considerably in recent years and the scope of innovation treatment has allowed a large number of patients the survival or function return to parts of the body affected [1, 2]. The body has the ability to defend itself from situations that are potentially capable of damaging it. Natural processes arising from this defence mechanism (partly controllable pharmacologically) can be a serious obstacle to the application of medical devices, as the body is not able to appreciate the benefits that they can derive. The fundamental problem resides in the fact that the acceptance (or rejection) of the body "extraneous" depends on the recognition of the nature of biocompatible materials by the tissues, rather than from the evaluation of the function performed. The body reacts to foreign materials of the tissues, rather than from the evaluation of the function performed. In the synthetic vascular prosthesis, for example, there is a risk that the blood clots on the inner surface of the occluding device making it useless (if not detrimental). Then a physiological phenomenon, essential for the survival of the organism, becomes potentially dangerous when the blood flows on surfaces that are not those with which is used to interact. It is important to know the *wet-ability* of the material to be implanted to see if it, interfacing with biological systems, can improve or detrimentally interfere with the physiological activities of the body;

favour or not, the epitaxial growth. The wet-ability is a very important property of materials and can be defined as the ability with which they can let wetting uniformly and in a stable manner from a liquid substance [3, 5]. The study of medical devices imposes therefore knowledge of synthetic materials and the biological ones, of course, are characterized by physical properties, chemical and mechanical properties significantly different. A material is said *biostable* when it is not altered by biological fluids, otherwise it is said *biodegradable* when it undergoes a chemical / physics change that alters or changes the properties [1, 2]. Depending on the material interaction / organization are divided into: Biohazards, Bioinert, Bioactive, Bioabsorbable. Finally according to the chemical nature the biomaterials analyzed in this work are:

- *Metals:* steels (AISI 316L, AISI 304), Palladium (Pd), Gold (Au), Silver (Ag), Ti₆Al₄V, Zinc (Zn).
- *Ceramics:* Al₂O₃, Diamond, SiO₂, Glassy Carbon (CVD), Silica, TiO₂.
- *Polymers:* Intraocular lens AcrySof IOL (PMMA based), polyethylene (PE), polymethylmethacrylate (PMMA), polytetrafluoroethylene or Teflon (PTFE), polylactic acid (PLA).

The ablation with laser pulses is a high-precision technology and spatial resolution which allows to obtain an efficient energy transfer without significantly damaging the surrounding material. The laser irradiation of material surfaces can affect changes in the materials wet-ability characteristics [6].

Materials and methods

In this work were measured and compared the angles of wet-ability of polymeric substrates, metallic and ceramic biocompatible materials. Will also consider the changes in the contact angles of four endodontic irrigants that best meet the requirements for optimal cleaning the root canal system (NICLOR 5, E.D.T.A PLUS, E.D.T.A 17%, HYPOCLEAN) of PMMA and a tooth transacted [8]. The main polymers used for the calculation of wet-ability in this work are: *Intraocular lens AcrySof IOL (PMMA based)*, *polyethylene (PE)*, *polytetrafluoroethylene or teflon (PTFE)*, *polylactic acid (PLA)*, *polymethylmethacrylate (PMMA)* [2]. The PMMA (polymethylmethacrylate) a thermoplastic acrylic resin obtained by the polymerization of free methyl methacrylate, is hard, relatively brittle but extremely abrasion resistant and stable when exposed to IR, UV, Visible radiations, possesses excellent properties of chemical resistance to the environmental conditions. In this work the polymer PMMA (dimension: 10mm × 4mm and of thickness 2mm) was irradiated in air by means of three types of laser sources operating in the UV, in the IR and visible regions. By variation of the laser energy and the number of shots was analyzed the variation of the wet-ability of this material surface. At the Department of Plasma Physics of the University of Messina has been used a Q-switched Nd:YAG laser at intensity of 10^9 W/cm² operating at the fundamental wavelength of 1064 nm, with pulse duration of 3 ns, energy of 180 mJ, which can operate in single shots and repetition rate (1 to 10 Hz). At the University Hospital of Messina in the Department of Surgical Specialties, UOC of Ophthalmology was used the UV-ArF excimer laser (Technolas 217Z100P) operating at the fundamental wavelength of 193 nm, characterized by a beam energy of 160 mJ with pulse duration of 18 ns with a Gaussian energy profile plate, working in single mode or repetition rate of 100 Hz. At the Dental Clinic of Catania has been used a diode laser (Lamba Scientific - D5-Doctor Smile) fundamental wavelength 810 nm, 5 W, pulse duration of 0.5 ns, CW. The effects of laser irradiation of PMMA surface with the three lasers on the wet-ability were measured before and after ablation. Metallic materials from equipment used for measuring wet-ability in this work are: *Gold, Silver, Palladium, Copper, Titanium, Austenitic Steels AISI 304 and AISI 316L and Titanium Alloy Ti₆Al₄V (TAV), Zinc (Zn)* [7]. The ceramics materials of which has been measured the angle of contact are: *Al₂O₃, Diamond, SiO₂, Glassy Carbon (CVD), Silica, TiO₂* [7]. To study the wet-ability of materials has been used the technique of the *sessile drop*, consisting in the measurement of "contact angle" between the tangent to the profile of a drop, deposited on the sample sur-

face, and the surface itself. The experimental setup which allows direct measurement of the contact angle consists of four elements:

- A mobile platform that houses the sample.
- An optical microscope.
- A webcam interfaced to a computer.
- A calibrated syringe that allows to deposit on the surface of the drops of liquid samples.

The webcam Philips CamSuite 2.0 is aligned to the eyepiece of the microscope and record the colour photo of the system formed by the solid sample and the drop. The eyepiece of the microscope has a resolution of 10× while the lens can vary between 4× and 2×. The images captured by the webcam has a resolution of 640 × 480 pixels and are processed by a computer with an image editing software (Photoshop CS4) and appropriate software for the measurement of angles (Golden Ratio). The software Golden Ratio, by the profile of the drop, is able to determine the contact angles of the left and right and the lengths of the drop. The platform moves horizontally and vertically to allow new evidence to a different pattern. The surface of the samples is cleaned with alcohol and dried with a stream of dry air. At a temperature of T=22°, a RH=35%, and at P=1atm, were performed on each sample 6 measurements of contact angle, which was subsequently averaged. As test liquid was used 1 of saline solution. The drop of saline solution placed on the surface of the sample will tend to widen when the surface is wettable (hydrophilic, $\theta < 90^\circ$), vice versa, will assume a spherical shape when the surface is non-wettable (hydrophobic, $\theta > 90^\circ$). For very small droplets the effect of distortion of gravity is minimal. The contact angle θ (degree) was calculated from the height h (mm) and the base diameter d (mm) of the droplet itself [3, 5]:

$$\theta = 2 \arctg\left(\frac{2h}{d}\right) \quad (1)$$

for $\theta < 90^\circ$, and

$$\theta = 90^\circ + \cos^{-1}\left(\frac{4hd}{4h^2 + d^2}\right) \quad (2)$$

for $\theta > 90^\circ$.

The determination of the contact angles for larger droplets is more complicated because the effect of gravity is not negligible and the drops are not spherical: in this case the measurement involves the measurement of the parameters that characterize the entire profile.

The parameters that influence the shape of drop at solid surface are:

- Solid-Liquid interfacial tension γ_{SL}
- Solid-Vapour interfacial tension $\gamma_{SV}(\gamma_S)$
- Liquid-Vapour interfacial tension $\gamma_{LV}(\gamma_L)$

These three parameters are linked with the contact angle θ by the Young equation [3, 5]:

$$-\gamma_{SV} + \gamma_{SL} + \gamma_{LV} \cos\theta = 0 \quad (3)$$

Solely γ_{LV} and θ are measurable, so additional equations are necessary to determine γ_{SL} and γ_{SV} . Several models were developed to calculate these parameters.

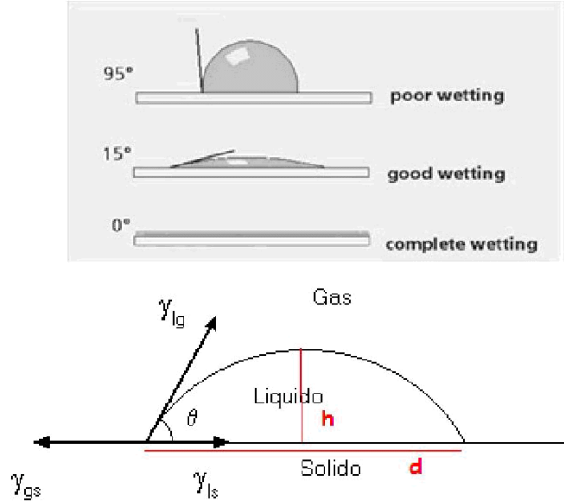


Figure 1: variation of wet-ability and technique of the sessile drop.

The variations that can be observed by measuring the contact angle of the saline solution on the samples prepared with various techniques in different environments can be attributed to the heterogeneity of the area determined by the roughness or from contamination.

The action of the environment is generally determined by the absorption of vapour on the polymer surface, effect which reduces the surface tension. There have been two theories to explain the effect of surface roughness on wet-ability. The first is described by Wenzel [3, 5]:

$$\cos\theta_W = r \cos\theta_Y \quad (4)$$

Where θ_W is the angle of effective contact of a rough surface real, or angle of Wenzel, r is the ratio between the actual area of the surface of the solid and the nominal one, and θ_Y is the contact angle of equilibrium of Young observed on a ideally smooth surface.

Since r is always greater than 1, this model provides an increase hydrophilicity ($\theta_W < \theta_Y$) to hydrophilic surfaces ($\theta_Y < 90^\circ$), and an increase in hydrophobicity ($\theta_W > \theta_Y$) to hydrophobic surfaces ($\theta_Y > 90^\circ$).

The second theory was derived by Cassie and Baxter, and assumes that the liquid substrate bathrooms completely wrinkled.

The expression proposed to describe this situation is given by the equation [3, 5]:

$$\cos\theta_{CB} = r_f f \cos\theta_Y + f - 1 \quad (5)$$

Where θ_{CB} is the angle of contact of Cassie-Baxter, f is the fraction of solid surface in contact with the liquid, and r_f is the ratio of the surfaces of the wet area and nominal.

When $f=1$ and $r_f = r$ the Cassie-Baxter equation is identical with the equation of Wenzel. Since f and r_f are always smaller than 1, the model of Cassie-Baxter expected that the increase of roughness of a surface face always increase the contact angle.

Results and Discussion

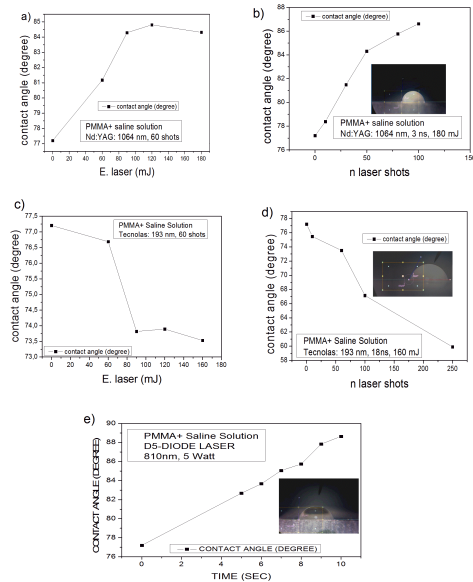


Figure 2: a) Trend contact angle of PMMA vs. energy Nd:YAG laser (60mJ - 90mJ - 120mJ - 180mJ); b) Trend PMMA contact angle vs. n laser shots Nd:YAG (10, 30, 60, 80, 100); c) Trend contact angle of PMMA vs laser energy Technolas (60mJ - 90mJ - 120mJ - 160mJ); d) Trend PMMA contact angle vs. n laser shots Technolas (10, 60, 100, 250); e) Trend contact angle vs. time PMMA laser pulse D5-Doctor Smile (5', 6', 7', 8', 9', 10').

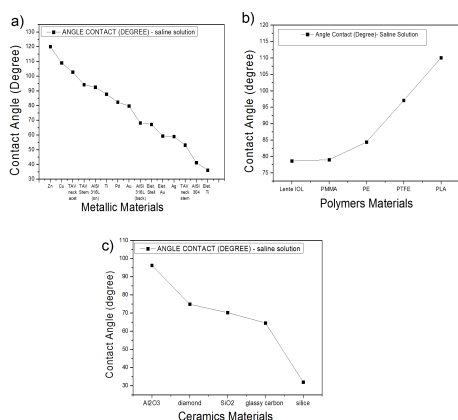


Figure 3: Contact angle a) metallic materials, b) polymeric and c) ceramics.

The PMMA was irradiated with three different sources initially by varying the laser energy from 60mJ to the maximum energy (180mJ for the Nd:YAG and 160 mJ for the Technolas) for 60 rounds and then instead maintaining maximum energy constant and varying the number of 10-250 laser shots.

With the laser diode, the sample was irradiated at maximum energy for different times (5 to 10 minutes). The variations of the wet-ability of the surface of the PMMA after laser treatment are shown in fig. 2. The contact angle on the target PMMA pure on which it was resting the drop of saline solution is approximately 77° . The action of UV laser (induces photothermal and photochemical effects: breakage of bonds, photodissociation [9, 10]), decreases the angle of wet-ability making the hydrophilic PMMA (incremental decrease of about -11°), while the lasers in the IR (which induces thermal effects) and in the Visible increase the wetting angle of making the hydrophobic PMMA (incremental change in contact angle of about $+7^\circ$ and $+17^\circ$ respectively) [6].

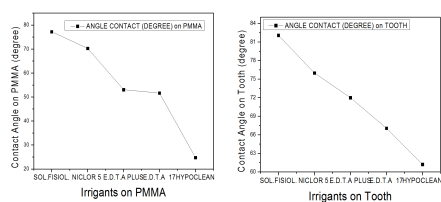


Figure 4: contact angle of dental irrigating of a) PMMA, on b) tooth.

The method of sessile drop has also allowed us to determine the variations of the angles of wet-ability of polymeric materials, metallic and ceramic. The trends of the above materials from the more hydrophobic (hardly wettable, $\theta > 90^\circ$) to the more hydrophilic (wettably easily, $\theta < 90^\circ$) are shown in the following figure 3. In the figure 4 are shown

the trends of the variation of the angle of contact of endodontic irrigants used in dentistry of PMMA and of the tooth. The contact angles of irrigants on PMMA are respectively found: NICLOR 5 ($\theta=70^\circ$); E.D.T.A PLUS ($\theta=53^\circ$); E.D.T.A 17% ($\theta=51^\circ$); HYPOCLEAN ($\theta=25^\circ$). The contact angle of irrigants on the tooth are: NICLOR 5 ($\theta=75^\circ$); E.D.T.A PLUS ($\theta=72^\circ$); E.D.T.A 17% ($\theta=67^\circ$); HYPOCLEAN ($\theta=61^\circ$).

Conclusion

In this work it has been demonstrated by varying the energy of the photons can be in control of the laser and therefore the energy deposited on the substrate. This result is extremely important in the medical field as it can modify the surface of the target by increasing or decreasing the contact angle and thus make it more hydrophilic or more hydrophobic. Were measured contact angles of the initial values of different polymeric materials, metallic and ceramic materials used in the medical field in the design of orthopedic implants, dental, ophthalmic, cardiac, for soft tissues. As reference liquid for the measurement of the angle of wet-ability in addition to the physiological solution and distilled water were considered four endodontic irrigants commonly used in dentistry that thanks to their ability to penetrate both the main and side channels, allow a cleansing optimal dentinal tubule both natural and artificial. The contact angle measurements are operator-dependent and can be influenced: by the preparation of the surface, from contamination from the environment, the temperature and the size of the droplet. These factors result in changes of surface roughness and / or modifications of the chemical properties of the surface and therefore significant changes in surface wet-ability. In order to modify the surface properties of biocompatible materials, we expect to treat them as well as with the laser also with chemical processes, thermal, ion implantation; while to modify its properties will send their internal electron beams and gamma rays.

References

- [1] Black, J.: *Biological performance of materials: fundamentals of biocompatibility*, New York: Marcel Dekker, 1999
- [2] Chiellini, E., et al.: *Biomedical polymers and polymer therapeutics*, New York-London: Kluwer Academic-Plenum Publishers, 2001
- [3] Mittal, K.L.: *Contact Angle, Wettability and Adhesion*, Brill, Leiden **6**, 2009
- [4] Kwok, D., et al.: *Contact angle measurements and contact angle interpretation. Contact angle*

- measurements by axisymmetric drop shape analysis and a goniometer sessile drop technique.* , Langmuir, **13**, 1997, p.2880-2894
- [5] Zisman, W.A.: *Contact angle, wettability and adhesion*, American Chemical Society, (43), 1964, p.1-51
- [6] De Marco, C., et al., *Surface properties of femtosecond laser ablated PMMA*, Applied Materials and Interfaces **2**, 2010, p.2377-2384
- [7] Ducheyne, P.: *Metal and Ceramic Biomaterials: Structure*, CRC Press,1984
- [8] Aktener, B.O., et al., *Smear layer removal with different concentrations of EDTA ethylenediamine mixtures* , Journal of Endodontics **19 (5)**, 1993, p.228-231
- [9] Torrisi, L., et al.: *Applicazioni di fasci laser al settore biomedico*. In Proceedings of X Giornata di Studio Bioingegneria, Catania, p. 22-35
- [10] Torrisi, L., et al.: *Laser Applications in Bio-Medical Field*. In Proceedings of : II Workshop PBSA,Lecce, pp.144-154

Volumetric Anomaly of a Gaussian Core Fluid on a Sphere

C. Speranza¹

¹ *Dipartimento di Fisica e di Scienze della Terra, Università degli Studi di Messina, Contrada Papardo, 98166 Messina, Italy*

E-mail: cristina.speranza@unime.it

Abstract

The thermodynamic and structural properties of the Gaussian-core model, with particular emphasis on its volumetric behavior, have been investigated in two dimensions in a system of particles moving on a sphere. The absence of an attractive term in the potential rules out the liquid-vapor phase transition while the curvature of the host surface inhibits the formation of a long-range-ordered crystalline arrangement. We found that the density exhibits, at moderate pressures, two extrema which delimit the temperature range where the thermal expansivity attains negative values. The presence of a density minimum has also been detected in the two-dimensional crystal on a plane.

Gaussian-core model, water-like anomalies, two-dimensional systems

Introduction

In this note I report on a computational study carried out on a fluid of Gaussian repelling particles hosted on a spherical surface [1], which generalizes a previous Monte Carlo analysis of the same model confined to one dimension [2].

The Gaussian-core model (GCM) [3–5] has been widely studied with both theoretical and computational methods because it can be used as a prototype system for some soft-matter polymeric materials. Moreover, its thermodynamic and structural properties recall in many aspects the behaviour of the most important complex fluid on the earth, *viz.*, water. This substance has a very special thermodynamic property that is shared by few other materials only: at ambient pressure, below 4°C and down to the freezing point, it expands upon cooling. According to some recent experimental and computational studies, the density maximum might be followed by a minimum at lower temperatures along the metastable branch of deeply supercooled water [6–9].

It is well known that particles interacting through isotropic core-softened potentials may display water-like anomalies, including a density maximum in the fluid phase [10, 11]. A density minimum has also been found in one-dimensional (1D) model fluids [2, 12, 13]. However, detecting this feature may be problematic in more realistic higher-dimensional systems because of intervening discontinuous phase transitions, typically freezing. In order to study this phenomenology in a more interesting scenario than that provided by the one-dimensional fluid, I investigated the GCM in two

dimensions but, to avoid the potential interference of a phase transition, particles were confined on a spherical surface which is known to frustrate the onset of long-range order. No density minimum had been observed so far in the fluid phase of the GCM, neither in three [4] nor in two dimensions [14].

It may be useful to note that simulating Gaussian repulsive particles embedded in a spherical surface may actually give information on the behaviour of real molecular substances in locally inhomogeneous conditions such as those that are typically found in the first hydration shell of a globular protein, like lysozyme or myoglobin.

Model and method

In this paper I present the results of an investigation carried out with the Monte Carlo (MC) method in the isothermal-isobaric ensemble, using spherical boundary conditions (SBC). The system was composed of $N = 500$ point particles repelling each other through a Gaussian pair potential $u(r) = \epsilon \exp(-r^2/\sigma^2)$, where r is the interparticle distance while ϵ and σ are the energy and length scales, respectively. As anticipated above, with regard to the melting transition there is an evident difference between the planar and the spherical system: while in the first case, the transition shows a thermodynamic singularity, as well as a reentrant melting, which is a characteristic of systems that interact through bounded potentials, in the second case the sharp transition is suppressed and becomes just a crossover phenomenon [15, 16].

The data were collected over an equilibrium trajectory of, typically, two million sweeps (every sweep consisting of N elementary MC moves). The simulations were carried out along selected isobaric paths, from high to low temperatures with a step $\Delta T^* = -0.0005$. In the following, I shall use reduced units for temperature, density and pressure: $T^* = k_B T / \epsilon$, $\rho^* = \rho \sigma^2$ and $P^* = P \sigma^2 / \epsilon$. Besides the particle number density ρ and the average energy per particle E/N , I computed the specific heat at constant pressure, $C_P = T(\partial s / \partial T)_P$, where s is the entropy per particle, the isothermal compressibility, $K_T = -v^{-1}(\partial v / \partial P)_T$, where $v = \rho^{-1}$ is the average volume per particle, and the thermal expansion coefficient, $\alpha_P = v^{-1}(\partial v / \partial T)_P$.

Simulation results

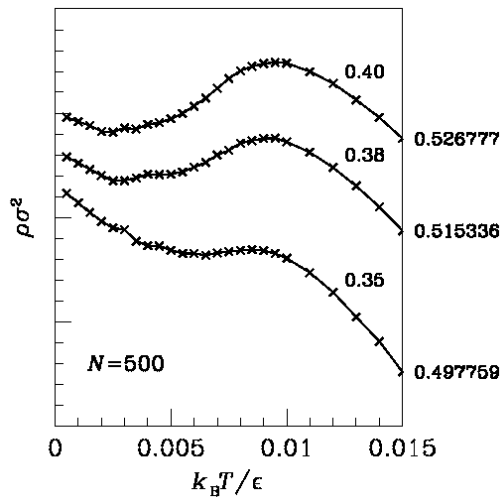


Figure 1: Reduced number density plotted as a function of the reduced temperature for increasing pressures $P^* = 0.35, 0.38, 0.40$. The curves were shifted along the vertical direction so as to make their main features more visible; the separation between two major tick marks along the left vertical axis is equal to 0.0005, while the absolute scale has been fixed through the value of each curve at $T^* = 0.015$ that is reported on the right vertical axis

The phase behavior of the system was investigated from low to high pressures, specifically in the range (0.3–2.0) and for reduced temperatures lower than 0.03.

As expected, the formation of long-range order is inhibited by the curvature of the sphere; hence, no thermodynamic response function exhibits a dis-

continuity. However, the density displays a non-monotonic trend when plotted as a function of the temperature, as shown in Fig.1 for three values of the pressure ($P^* = 0.35, 0.38, 0.40$), where a maximum is followed by a shallow minimum at lower temperatures. While a maximum in the density of the GCM fluid had already been observed in three [17] as well as in two dimensions [14], the appearance of a minimum is a novel finding.

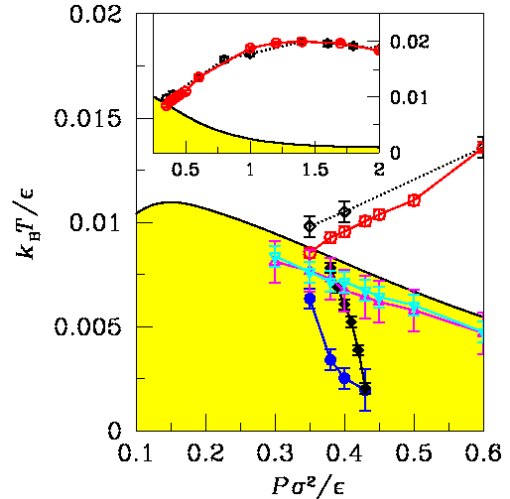


Figure 2: Location of the density and thermodynamic response functions extrema in the P - T plane. We used polynomial interpolations to locate maxima and minima. Black line: melting line of the planar GCM system (the solid phase is stable at lower temperatures); open circles: temperatures of maximum density (TMD) on the sphere; open diamonds: TMD line of a planar GCM fluid; solid circles: temperatures of minimum density (TmD) on the sphere; solid diamonds: TmD line of the planar GCM solid; open triangles: temperatures of minimum thermal expansivity; open inverted triangles: temperatures of maximum isobaric specific heat. The inset shows the TMD lines for the fluid on the sphere and for the planar GCM fluid, plotted over a more extended pressure range. Lines traced through the data points are a guide to the eye

The anomalies observed in the other thermodynamic response functions are all a consequence of the volumetric anomaly [2]. Both α_P and C_P show a minimum and a maximum, respectively, along an isobaric path. However, at variance with the results found in the one-dimensional system, I could not detect a maximum in the isothermal compressibility because of its low rate of change as a function of temperature and of the statistical noise of the data. The loci of the extrema of ei-

ther the density or of a thermodynamic response function are reported in the P - T plane in Fig. 2. Note that the lines traced by the isobaric minimum of the thermal expansivity and by the isobaric maximum of the specific heat run very close to each other and, in analogy to what happens in one-dimension, cross the boundary of the density-anomaly region at the point of confluence of the lines generated by the density maximum and minimum, respectively.

Finally, the volumetric behavior of the Gaussian fluid in a spherical geometry was compared with that of the corresponding flat system. The results of the MC simulations for $N = 1152$ particles did not show any particular feature along the fluid branch; conversely, over a narrow pressure range ($0.38 \leq P^* \leq 0.43$), the number density of the triangular solid exhibits a minimum. As can be seen from Fig. 2, the locus of such minima runs very close to the density-minima locus of the spherical GCM fluid.

Conclusions

In the study that forms the object of this note I investigated the thermodynamic behaviour of the Gaussian-core model in two dimensions with spherical boundary conditions. Under such conditions, the GCM exhibits a two-fold volumetric anomaly that is somehow reminiscent of that found in metastable supercooled water confined inside nanocylinders. The density anomaly range is bounded at high temperatures by a locus of maxima and, at low temperatures, by a locus of minima. Both such lines stem from a common point C, where both the first and second temperature derivatives of the density vanish. I have also identified the lines of maximum isobaric specific heat and of minimum thermal-expansion coefficient which cross the boundary of the anomalous density region at C.

Interestingly, the density minima locus that is also present in the crystalline phase of the flat GCM runs close to the corresponding locus of the system in curved geometry, a circumstance which strongly suggests that this feature may have its roots in the very nature of the potential as well as in the *local* spatial arrangements that it generates at low temperatures and high pressures.

References

- [1] S. Prestipino, C. Speranza, and P. V. Giaquinta, "Density anomaly in a fluid of softly repulsive particles embedded in a spherical surface", *Soft Matter* (2012); DOI: 10.1039/c2sm26706c.
- [2] C. Speranza, S. Prestipino, and P. V. Giaquinta, "Thermodynamic and structural anomalies of the Gaussian-core model in one dimension" *Mol. Phys.* **109**, 3001 (2011); DOI: 10.1080/00268976.2011.628342.
- [3] F. H. Stillinger, *J. Chem. Phys.* **65**, 3968 (1976).
- [4] S. Prestipino, F. Saija, and P. V. Giaquinta, *Phys. Rev. E* **71**, 050102(R) (2005).
- [5] P. V. Giaquinta and F. Saija, *ChemPhysChem* **6**, 1768 (2005).
- [6] P. W. Bridgman, *Proc. Amer. Acad. Arts Sci.* **47**, 441 (1912).
- [7] C. A. Angell et al., *Phys. Chem. Chem. Phys.* **2**, 1559 (2000).
- [8] D. Liu, Y. Zhang, C.-C. Chen, C.-Y. Mou, P. H. Poole, and S.-H. Chen, *Proc. Nat. Acad. Sci. U.S.A.* **104** 9570 (2007).
- [9] F. Mallamace et al., *Proc. Natl. Acad. Sci. U.S.A.* **104**, 18387 (2007).
- [10] G. Malescio, F. Saija, and S. Prestipino, *J. Chem. Phys.* **129**, 241101 (2008).
- [11] See S. V. Buldyrev et al., *J. Phys.: Condens. Matter* **21**, 504106 (2009) and references therein.
- [12] M. R. Sadr-Lahijany et al., *Phys. Rev. E* **60**, 6714 (1999).
- [13] A. Ben-Naim, *J. Chem. Phys.* **128**, 024505 (2008).
- [14] S. Prestipino, F. Saija, and P. V. Giaquinta, *Phys. Rev. Lett.* **106**, 235701 (2011).
- [15] S. Prestipino Giarritta, M. Ferrario, and P. V. Giaquinta, *Physica A* **187**, 456 (1992).
- [16] S. Prestipino Giarritta, M. Ferrario, and P. V. Giaquinta, *Physica A* **201**, 649 (1993).
- [17] See, e.g., P. Mausbach and H.-O. May, *Fluid Phase Equil.* **249**, 17 (2006).

THIRD YEAR

PhD STUDENTS

CYCLE XXV

Energy shift and field enhancement in dye-coated plasmonic nanoparticles

A. Cacciola¹

¹*Dottorato di Ricerca in Fisica, Dip.t di Fisica e Scienze della Terra, Viale F. Stagno d' Alcontres, 98166 S. Agata-Messina, Italy*

E-mail: acacciola@unime.it

Abstract

We study the optical response of dye-coated plasmonic nanoparticles, made of gold dimers coated with methylene blue molecules. The optical properties of such composite nanoparticles are explored through a computational approach based on the multipole expansions of the electromagnetic fields and the Transition matrix. We find that the interaction between the gold nanoparticle plasmons and the dye resonances dramatically changes the surface enhanced Raman scattering spectrum of the system. We also present a comparison with experimental data.

Keywords: plasmon resonance, field enhancement, nanoparticles, Transition matrix.

Introduction

Over the past decade, there has been a large amount of interest in plasmonic applications of metal nanoparticles (MNPs) in biology, medicine, spectroscopy and many other fields. These applications rely on the fact that MNPs support localized surface plasmon resonances, which are the collective coherent oscillations of the nanoparticle free electrons (with respect to the positive metallic background) in resonance with an electromagnetic wave. The plasmon resonance results in a large enhancement of the electromagnetic field around the nanoparticle, resulting in a strong light absorption and scattering at the plasmon resonance frequency [1, 2]. Although extinction, absorption, and scattering are still the primary optical properties of interest, other spectroscopic techniques, e.g. surface enhanced Raman scattering (SERS), are sensitive to the electromagnetic fields at or near the particle surfaces, thus providing important new challenges for theory.

This work finds its motivation in the interpretation of SERS spectra of gold nanoparticles, coated with methylene blue (MB) molecules, and deposited on a glass substrate. The plasmon enhancement in these near-field spectra appears red-shifted compared with the far-field measures of plasmon resonance. We investigate this behaviour through a computational approach based on the multipole expansions of the electromagnetic fields and the Transition matrix (T-matrix) method [3].

In this paper we will briefly introduce the computational method that we use, and then we will present our computational results and a comparison with experimental data. We will finally draw some conclusions and briefly discuss future perspectives.

The Transition matrix method

We study the optical behaviour of metal nanoparticles, both isolated or clustered, through the multipole expansions of the electromagnetic fields within the T-Matrix method. This is a general approach that applies to particles of any shape and refractive index and for any choice of the radiation wavelength.

Expanding the incident field in a series of vector spherical harmonics with known amplitudes $W_{l\eta lm}^{(p)}$, the scattered field can be expanded on the same basis with amplitudes $A_{\eta lm}^{(p)}$. The relation between the amplitudes of scattered and incident field is given by [4]

$$A_{\eta lm}^{(p)} = \mathcal{S}_{lm'l'm'}^{(pp')} W_{l\eta l'm'}^{(p')}. \quad (1)$$

The elements of the T-matrix $\mathcal{S}_{lm'l'm'}^{(pp')}$ encompass all the information on the morphology and orientation of the particle with respect to the incident field. The elements of the T-Matrix are calculated in a given frame of reference through the inversion of the matrix of the linear system obtained by imposing the boundary conditions to the fields across each spherical surface of the scatterers.

The T-matrix approach presents invaluable advantages when dealing with the properties of dispersions of particles whose orientational distribution is known because the T-matrix has well defined transformation properties under rotation that permit a straightforward (analytical) evaluation of orientational averages [3]. In fact, as we are interested in the optical properties of dispersions as a whole, we exploit these properties assuming a random orientational distribution. The analytical evaluation of the averages produces a much improved accuracy of the solution and results in a remarkable reduction of CPU

time.

The procedure devised for the extension of the T-Matrix formalism to the study of the optical behaviour of an aggregate of N , not necessarily equal, spheres whose mutual distances are so small that the interaction effects cannot be neglected can be found in [3]. In such case the T-Matrix approach allows to take proper account of the multiple scattering processes among the spheres composing the aggregate. The number of subunits in the aggregate are limited only by the memory demand of the computing facilities.

Results and discussion

We model our system as a gold dimer coated with MB, a dye which is optically active in the same frequency range of the gold plasmon. The dimer is composed of two identical spherical subunits in contact, embedded in a medium with refractive index $n = 1$. Each subunit has a core-shell structure with a radius of 12 nm. The gold core has a radius of 5 nm, the first silica shell has a thickness of 1 nm, and the external MB shell has a thickness of 6 nm. The incident field is perpendicular to the dimer axis, the field polarization is parallel to the dimer axis. The choice of this model finds its motivation in the analogy with the experimental samples. In our computations we describe the optical behaviour of gold nanoparticles using the dielectric function given by Johnson and Christi [5]. Table 1 summarizes the absorption maxima observed in the visible absorption spectra of MB species corresponding to different states of aggregation of the molecules [6].

absorption max/nm	adsorbed species	assignment
570	$(MB)_3$, MB_n	trimer and higher aggregates
600-610	MB, $(MB)_2$	monomer and H-dimer
653	MB	monomer
670	MB	monomer
720	$(MB)_2$	L-dimers
760	MBH_2^+	protonated methylene blue

The experimental dielectric constant for MB appears to be inadequate to reproduce these observed features [7]. Therefore we use an effective dielectric function to simulate the observed absorption spectra. In Figure 1 we compare the bulk experimental dielectric function (bullets) and the effective one (solid line) that takes account of the different molecules aggregation states.

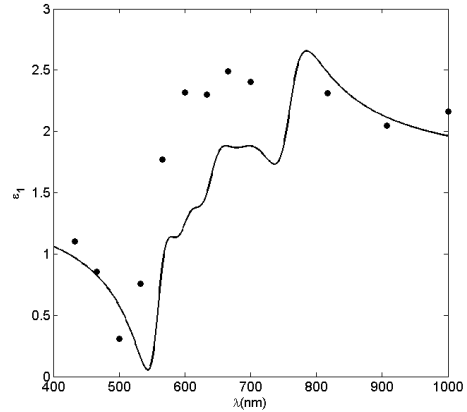


Figure 1: Bulk experimental dielectric function (bullets) and effective dielectric function for MB (solid line)

In Figure 2 we show the theoretical enhancement factor computed according to the definition by Novotny and Hecht [8] for incident laser beams with different wavelengths in the visible range. The near field quantities are computed at the contact point between the dimer subunits, that is in the hot spot region where the field enhancement has its maximum values. We can notice that the enhancement factor is lower in the first part of the visible range (around 530 nm). Then we observe a steep rise in the enhancement factor at 650 nm, and finally a plateau at longer wavelengths. At first glance, this is a surprising behaviour. Since the gold plasmon resonance appears at 530 nm, we would expect to find the highest enhancement factor at this wavelength. Our computational data, shown in Figure 2, appear red-shifted compared with the wavelength of the plasmon resonance. This clearly indicates that the presence of the gold plasmon resonance is not sufficient to explain the behaviour of the enhancement factor.

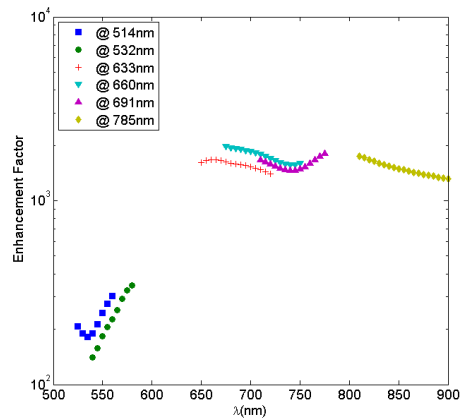


Figure 2: Computed enhancement factor for the model dimer

For a better understanding of this effect we extend our investigation to the optical behaviour of the dimer in the far field region. As we can see from Figure 3 (solid line), in far field the optical properties are sensitive almost entirely to the plasmon resonance. This implies that the high enhancement factor that we observe at wavelengths red-shifted compared with the plasmon resonance wavelength is a near-field effect. In order to confirm our interpretation, we compare our numerical results with observed extinction spectra (dashed line in figure 3) obtained for gold nanostructures deposited on a glass substrate. Such nanostructures are covered by a thin shell of silica and by an external layer of MB. The TEM images show that no clusterization appears in the sample and that the largest size of these gold nanostructures is less than 30 nm. Figure 3 shows that the measured extinction is quite in agreement with the computed one. We can observe that the plasmon computed peak is blue-shifted in comparison with the measured peak. This effect may arise as a consequence of the cooperative effect of the gold nanostructures interacting on the glass substrate.

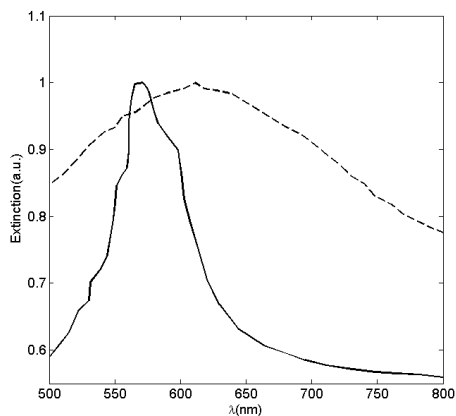


Figure 3: Computed extinction cross sections (solid line) for the model core-shell dimer compared with extinction of the experimental sample (dashed line)

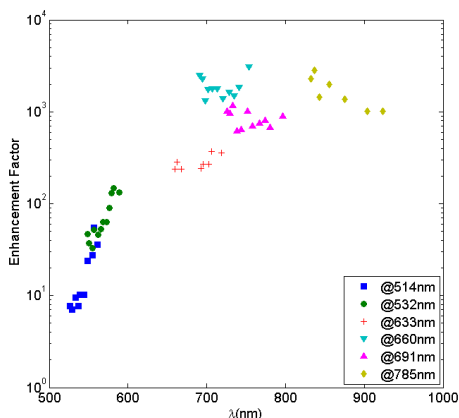


Figure 4: Experimental enhancement factor for the sample [9]

To further investigate this effect we performed many calculations changing the dimension and the core-shell composition of the dimer. In all the examined cases we find that the presence of MB molecules changes dramatically the enhancement factor behaviour because of the strong coupling between the MB resonances and the gold plasmon. When the MB shell is removed, the enhancement appears only around the plasmon peak at about 530 nm. In Figure 4 we show the enhancement factor measured by a SERS experiment [9]. The agreement with the computed enhancement factor shown in Figure 2 is very good, thus confirming the reliability of our computational results.

Conclusions

In conclusion, using the T-matrix approach and a suitable dimer model, we are able to simulate the SERS spectra of gold nanoparticles, coated with methylene blue (MB) molecules, and deposited on a glass substrate. The highest enhancement factor measured by the SERS experiment for this sample appears red-shifted compared with the gold plasmon resonance in far-field spectra. Our interpretation of this effect is based on the strong coupling between the MB resonances and the gold plasmon. The novel result of this work is that the effect of the MB molecules cannot be neglected in the interpretation of the SERS spectra. In order to generalize these results and to provide a systematic study of the interaction existing between nanoparticle plasmons and dye resonances, it is necessary to extend the investigation to other dyes. We expect that taking into account this interaction might provide improvements in understanding and optimising surface-enhanced spectroscopies.

Acknowledgements

I wish to thank R. Saija, M.A. Iatì, F. Borghese, P. Denti, P.G. Gucciardi, B. Fazio, A. Irrera, C. D'Andrea, and O.M. Maragò for fruitful discussions and support.

References

- [1] Maier, S.A.: *Plasmonics: Fundamentals and Applications*. New York: Springer, 2007
- [2] Quinten, M.: *Optical Properties of Nanoparticle Systems*. Weinheim: Wiley-VCH, 2011
- [3] Borghese, F., Denti, P., Saija, R.: *Scattering from*

- Model Nonspherical Particles*. Berlin: Springer-Verlag, 2007
- [4] Waterman, P.C.: *Symmetry, Unitarity, and Geometry in Electromagnetic Scattering*. Physical Review D, **3**, 1971, p. 825–839
- [5] Johnson, P.B., Christi, R. W.: *Optical Constants of the Noble Metals*. Physical Review B, **6**, 1972, p. 4370–4379
- [6] Nicolai, S.H.A., Rubim, J. C.: *Surface-Enhanced Resonance Raman (SERR) Spectra of Methylene Blue Adsorbed on a Silver Electrode*. Langmuir, **19**, 2003, p. 4291–4294
- [7] Egan, W.G.: *Optical Remote Sensing: Science and Technology*. CRC Press, 2004
- [8] Novotny, L., Hecht, B.: *Principles of Nano-Optics*. Cambridge University Press, 2006
- [9] D'Andrea, C., et al.: in preparation